Clays and Clay Minerals, Vol. 57, No. 2, 183–193, 2009.

CRYSTALLOGRAPHIC FEATURES AND CLEAVAGE NANOMORPHOLOGY OF CHLINOCHLORE: SPECIFIC APPLICATIONS

GIOVANNI VALDRÈ[1], DANIELE MALFERRARI[2], AND MARIA FRANCA BRIGATTI[2,*]

[1] Dipartimento di Scienze della Terra e Geologico-Ambientali, Università di Bologna, Piazza Di Porta S. Donato 1, I-40127 Bologna, Italy

[2] Dipartimento di Scienze della Terra, Università di Modena e Reggio Emilia, Largo S. Eufemia 19, I-41100 Modena, Italy

Abstract—Natural and synthetic micas have been used widely as substrates to study biological systems; but, as in the case of negatively charged DNA, anionic charge repulsion may render micas a less than ideal templating surface for many biological systems. The purpose of this study was to investigate the potential for the chlorite clinoclore, which contains a positively charged interlayer octahedral sheet, to serve as a substrate for DNA adsorption. The relationships between clinochlore cleavage characteristics, in terms of nano-morphology, and surface potential are investigated, as are its average crystal chemistry and topology. That the structural features of clinochlore can be used successfully to condense, order, and self assemble complex biomolecules, such as DNA is also proven.

A natural II*b*-4 clinochlore [$C\bar{1}$ symmetry, unit-cell parameters a = 0.53301(4); b = 0.92511(6); c = 1.4348(1) (nm); α = 90.420(3); β = 97.509(3); γ = 89.996(4) (º)] with chemical composition ($Mg_{1.701}Fe^{2+}_{0.245}Ti_{0.004}Al_{0.998}Cr^{3+}_{0.052}$) Mg_3 ($Si_{2.939}$ $Al_{1.015}$ $Fe^{3+}_{0.046}$)$O_{10}(OH_{7.913}F_{0.087})$ was selected. The octahedral sites of the silicate layer (<*M*(1)–O> = 0.2080 nm and <*M*(2)–O> = 0.2081 nm) are equal and occupied by Mg, whereas the octahedral sites in the interlayer *M*(3) and *M*(4) (<*M*(3)–O> = 0.2088 nm and <*M*(4) – O> = 0.1939 nm) show different sizes and are mostly completely occupied by divalent (Mg^{2+} and Fe^{2+}) and trivalent (Al^{3+}) cations, respectively.

The clinochlore cleaved surface is present in two forms: (1) the stripe type (0.40 nm in height, up to several micrometers long and ranging from some nanometers to a few microns in lateral size); and (2) the triangular type (0.40 nm in height). Both features may result either from interlayer sheets whose cleavage weak directions are related to the different *M*(3) and *M*(4) site occupancy, or from weak interlayer bonding along specific directions to the 2:1 layer underneath. The cleaved surface, particularly at the cleaved edges, presents high DNA affinity, which is directly related to an average positive surface and ledge potential.

Key Words—AFM, Clinochlore, Crystal Structure, Surface Applications, XAS.

INTRODUCTION

Phyllosilicates, such as natural and synthetic micas, are used widely as substrates to study biological systems such as DNA. The DNA molecules, attached to the mineral surface as a one-molecule thick layer, show mean dimensions much larger than the roughness of the cleavage plane (*i.e.*, the negatively-charged basal oxygen plane) and thus can be easily identified via atomic force microscopy (AFM) investigations (Bustamante *et al.*, 1992; Vesenka *et al.*, 1992; Klinov *et al.*, 2006; Sushko *et al.*, 2006).

Other phyllosilicates, such as chlorite (Valdrè *et al*., 2004; Valdrè, 2005; Valdrè, 2007; Antognozzi *et al.*, 2006), are promising alternatives to micas. Chlorite consists of two polyhedral units, *i.e.* (1) a 2:1 layer of two tetrahedral sheets sandwiching an octahedral sheet; and (2) an octahedral, usually brucite-like, interlayer (Bailey, 1988). The chlorite cleavage surface is either the interlayer octahedral (brucite-like) sheet, which is usually positively charged due to isomorphous substitution, or the tetrahedral basal oxygen plane. Thus, unlike mica that presents only negatively charged surfaces (*i.e.* the tetrahedral basal oxygen plane), chlorite produces a surface that is either positively or negatively charged. For DNA, a negative charge results from two ionized oxygen atoms per base along the length of the double helix (Ha and Liu, 1997). Compared to mica, therefore, the attraction between DNA and chlorite brucite-like surfaces is greater.

Identification of the arrangement of organic molecules on mineral surfaces by AFM requires the proper characterization of the interactions that occur on these surfaces. These interactions depend on chemical composition, atomic structure, polytypic arrangement (Downs and Hazen, 2004), topographic features (Joshi *et al.*, 1970; Joshi and Paul, 1977; Theng *et al.*, 1998), and electrochemical properties, such as surface potential (Parsons, 1990).

In the present study, (1) the crystal structure of a clinochlore from Rocca Sella, Val di Susa, (western Alps, Italy), is characterized; (2) the crystal chemical properties are related to the cleavage patterns and roughness, and (3) the crystal chemical and surface properties (nano-morphology and potential) are related to the deposition of organic molecules, such as DNA.

* E-mail address of corresponding author:
brigatti@unimore.it
DOI: 10.1346/CCMN.2009.0570205

EXPERIMENTAL METHODS

Chemical analysis

A natural clinochlore from Rocca Sella, Val di Susa (western Alps), Italy, was selected. The sample consists of green, platy clinochlore crystals coexisting with calcite, perovskite, and magnetite. The chemical composition of the clinochlore was obtained by combining: (1) the average of six microprobe point analyses, determined by wavelength-dispersive electron microprobe analysis (ARL-SEMQ electron microprobe, working conditions 15 kV and 15 nA, beam size 8−15 μm, counting times of 10 s for both peak and background); (2) H_2O determination evaluated by thermal analysis (Seiko SSC 5200 thermal analyzer equipped with GeneSys ESS Quadstar 422 mass spectrometer at heating rate of 10ºC/min in He gas flow, flowing rate of 100 μL/min); and (3) information on the Fe oxidation state obtained by the sodium metafluoroborate method of Meyrowitz (1970). The composition (wt.%) is: MgO 33.41(15), TiO_2 0.06(2), Cr_2O_3 0.70(3), FeO 3.10(15), Fe_2O_3 0.64, Al_2O_3 18.10(48), SiO_2 31.13(48), F 0.29(7), H_2O 12.50, total 99.93.

The chemical formula was derived by normalization, where: (1) the positive charges were balanced to 10 oxygen atoms and 8 (OH, F) atoms; (2) tetrahedral sites were considered to be filled with Si, Al, and Fe^{3+} (based on X-ray absorption spectroscopy (XAS) analyses, see below) to an occupancy of 4.0 atoms per formula unit (a.p.f.u.); (3) the octahedral sites were filled with Al, Ti, Cr, Mg, Mn, and Fe. The formula determined is: $(Mg_{1.701}Fe^{2+}_{0.245}Ti_{0.004}Al_{0.998}Cr^{3+}_{0.052})Mg_3(Si_{2.939}Al_{1.015}Fe^{3+}_{0.046})O_{10}(OH_{7.913}F_{0.087})$, and the sample is a clinochlore (Bayliss, 1975).

Single crystal X-ray diffraction (SC-XRD)

The clinochlore crystal (space group $C\bar{1}$; II*b*-4 polytype; 0.11 mm × 0.10 mm × 0.04 mm in size), selected for structural investigation, was mounted on a Bruker X8-Apex fully automated four-circle diffractometer with Kappa geometry, ceramic X-ray tube KFF-Mo-2k-90 Fine Focus, and *APEX* 4K CCD area detector. Three sets of 12 frames were used for the initial unit-cell determination, each frame being measured with 0.5ºφ rotation and 10 s of exposure time. The crystal-to-detector distance was 40 mm and the collection strategy was optimized by the *APEX* program suite (Bruker, 2003a). The semi-empirical absorption correction (*SADABS*) was based on fitting a function to the empirical transmission surface as sampled by multiple equivalent measurements (Sheldrick, 2005). The *SAINT-IRIX* (Bruker, 2003b) package was used for data reduction and unit-cell refinement. Unit-cell parameters and details of data collection and refinement are listed in Table 1.

The crystal structure was refined using the *SHELX*-97 package of programs (Sheldrick, 1997), starting from the

Table 1. Miscellaneous information pertaining to the structure refinement and unit-cell parameters for clinochlore-II*b*-4.

Crystal system	Triclinic
Space group	$C\bar{1}$
Crystal size	0.10 mm × 0.11 mm × 0.04 mm
Cell parameters	a = 0.53301(4), b = 0.92511(6), c = 1.4348(1) nm, α = 90.420(3), β = 97.509(3), γ = 89.996(4)º
Volume	0.70140(9) nm^3
Radiation type	MoKα
Data collection wavelength	0.071073 nm
Monochromator	Graphite
Measurement method	φ and ω scan
Adsorption correction	Bruker *SADABS*
Reflections collected	4289
Independent reflections	2392 (R_{int} * = 0.0232)
θ_{min}	4.30º
θ_{max}	39.18º
Miller index limits	$-9 \leqslant h \leqslant +9$ $-15 \leqslant k \leqslant +15$ $-21 \leqslant l \leqslant +25$
Refinement method	Full-matrix least-squares on F^2
Parameters refined	146
R indices [$F_0 > 2\sigma(F_0)$]	$R(F)^{\ddagger}$ = 0.0362; w$R(F^2)^{\S}$ = 0.0814
R indices (all data)	R(F) = 0.0471; w$R(F^2)$ = 0.0835
GoF†	0.943

* $R_{int} = \Sigma|F_o^2 - F_o^2(mean)|/\Sigma[F_o^2]$

‡ $R(F) = \Sigma||F_o| - |F_c||/\Sigma|F_o|$

§ $wR(F^2) = \{\Sigma[w(F_o^2 - F_c^2)^2]/\Sigma[w(F_o^2)^2]\}^{1/2}$; w = $1/[\sigma^2(F_o^2) + (aP)^2 + bP]$ where P is [$2F_c^2$ + Max(F_o^2, 0)]/3

† GoF = S = $\{\Sigma[w(F_o^2 - F_c^2)^2]/(n - p)\}^{1/2}$

https://doi.org/10.1346/CCMN.2009.0570205 Published online by Cambridge University Press

atomic coordinates of Joswig and Fuess (1990) and using atomic scattering factors and $\Delta f'$, $\Delta f''$ coefficients from the *International Tables for Crystallography* (Wilson and Prince, 1999). The electron density in the octahedral *M*(1), *M*(2), and *M*(3) cation sites was determined by fitting the scattering factor curves of Mg^{2+} and Fe^{2+} with variable occupancy; in the *M*(4) octahedron the scattering factor curves of Al^{3+} and Fe^{2+} were assumed, whereas a composite of 75% Si^{4+} , 20% Al^{3+}, 5% Fe^{3+} was set for tetrahedral sites. Full occupancy was assumed for all cation sites. Octahedral mean electron counts from crystal structure refinements were in good agreement with the chemical analysis.

The hydrogen atoms were located in the difference electron density map and included in the last cycles of refinement, with equal isotropic atomic displacement parameters. At the end of the refinement, the calculated difference electron density map revealed no significant excess electron density above background. Tabulated parameters included atomic coordinates and equivalent isotropic and anisotropic displacement factors (Table 2), interatomic distances and structural parameters derived from the crystal structure refinement (Table 3), and the observed and calculated structure factors (Table 4, deposited at http://www.clays.org/journal/JournalDeposits.html).

X-ray absorption spectroscopy (XAS)

Fe *K*-edge XAS spectra were collected at the European Synchrotron Radiation Facility (ESRF, Grenoble, France) on the Spanish Beam Line (SpLine, BM25 Branch A). The storage ring conditions were 6 GeV working in the current range 180−200 mA. A Si(111) double-crystal monochromator was used, providing an energy resolution of ~0.4 eV at the Fe *K*-edge, which is much less than the Fe *K* natural line width (~1.15 eV; Krause and Oliver, 1979). For all spectra, a metallic Fe reference foil was used to provide an energy calibration for the monochromator (energy reproducibility: ±0.05 eV). Data were collected in fluorescence mode at room conditions. The spectra were recorded over a range of 500 eV across the Fe absorption *K*-edge with a 1 eV energy step in the X-ray absorption near-edge structure (XANES) region (7100−7150 eV) and 3 eV in the extended X-ray absorption fine structure (EXAFS) region (7150−7500 eV). Tetra-ferriphlogopite and annite were used as analogs to interpret the clinochlore XAS spectra. Both minerals are well characterized phyllosilicates (Giuli *et al*., 2001; Tombolini *et al*., 2002), with talc-like characteristics and which contain mainly Fe^{3+} in tetrahedral coordination (tetra-ferriphlogopite) and Fe^{2+} in octahedral coordination (annite).

Scanning probe microscopy (SPM)

A Nanoscope III Multimode SPM device (Digital Instruments, Santa Barbara, California) was used to investigate the electrostatic interactions between the probe and the sample surface. For dynamic-mode electric force microscopy (EFM), amplitude, frequency, and phase-modulation imaging were performed using NCHPt NanoWorld (Switzerland) Pt-Ir-coated silicon tips ($k \approx 40$ N/m, working frequency ≈ 270 kHz).

In static-mode EFM, the experiments were performed in Force Volume operative mode, by which a

Table 2. Atomic coordinates and equivalent and anisotropic displacement parameters ($nm^2 \times 10^5$) of clinochlore-II*b*-4.

Atom	*x*	*y*	*Z*	U_{eq}	U_{11}	U_{22}	U_{33}	U_{23}	U_{13}	U_{12}
M(1)	0	0	0	9(1)	7(1)	8(1)	13(1)	0(1)	1(1)	1(1)
M(2)	0.0016(1)	0.3338(1)	1.0000(1)	10(1)	7(1)	8(1)	13(1)	0(1)	1(1)	1(1)
M(3)	0.9994(1)	0.1668(1)	0.5000(1)	11(1)	8(1)	9(1)	17(1)	0(1)	2(1)	0(1)
M(4)	0	0.5	0.5	9(1)	6(1)	7(1)	13(1)	0(1)	1(1)	0(1)
Si(1)	0.2333(1)	0.1696(1)	0.1931(1)	8(1)	6(1)	7(1)	12(1)	0(1)	1(1)	0(1)
Si(2)	0.7342(1)	0.0029(1)	0.1931(1)	8(1)	6(1)	7(1)	12(1)	0(1)	1(1)	0(1)
OH(1)	0.6921(2)	0.3342(1)	0.0737(1)	12(1)	10(1)	11(1)	13(1)	0(1)	1(1)	0(1)
OH(2)	0.1633(2)	0.9986(1)	0.4301(1)	12(1)	12(1)	13(1)	12(1)	0(1)	1(1)	−1(1)
OH(3)	0.1312(2)	0.3426(1)	0.4300(1)	12(1)	11(1)	12(1)	13(1)	0(1)	1(1)	−1(1)
OH(4)	0.6315(2)	0.1550(1)	0.4307(1)	12(1)	10(1)	14(1)	12(1)	0(1)	1(1)	2(1)
O(1)	0.1934(2)	0.1677(1)	0.0770(1)	10(1)	7(1)	9(1)	14(1)	0(1)	1(1)	0(1)
O(2)	0.6939(2)	1.0014(1)	0.0770(1)	11(1)	8(1)	11(1)	13(1)	−1(1)	1(1)	0(1)
O(3)	0.2050(3)	0.3376(1)	0.2347(1)	18(1)	22(1)	13(1)	18(1)	0(1)	4(1)	−1(1)
O(4)	0.5204(2)	0.1087(2)	0.2347(1)	17(1)	13(1)	21(1)	17(1)	−1(1)	1(1)	3(1)
O(5)	0.0202(3)	0.0652(2)	0.2345(1)	17(1)	14(1)	21(1)	16(1)	1(1)	1(1)	−3(1)
H(1)	0.681(7)	0.343(5)	0.140(3)	31(6)						
H(2)	0.144(7)	0.996(5)	0.369(3)	27(7)						
H(3)	0.102(6)	0.341(4)	0.366(2)	26(5)						
H(4)	0.600(8)	0.153(4)	0.369(3)	36(7)						

U_{eq} is defined as one third of the trace of the orthogonalized U_{ij} tensor. The anisotropic displacement factor exponent takes the form: $\exp -2\pi^2[h^2 (a^*)^2 U_{11} + ... + 2hka^*b^* U_{12} + ...]$. Estimated standard deviations refer to the last digit.

https://doi.org/10.1346/CCMN.2009.0570205 Published online by Cambridge University Press

Table 3. Values of interatomic distances (nm) and selected parameters for clinochlore-II*b*-4.

	Distance		Distance
Tetrahedron *T*(1)		Tetrahedron *T*(2)	
T(1)−O(1)	0.1651(1)	*T*(2)−O(2)	0.1651(1)
T(1)−O(5)	0.1662(2)	*T*(2)−O(3)	0.1661(1)
T(1)−O(4)	0.1668(1)	*T*(2)−O(5)	0.1664(2)
T(1)−O(3)	0.1674 (1)	*T*(2)−O(4)	0.1669(1)
<*T*(1)−O>	0.1664	<*T*(2)−O>	0.1661
τ	110.76(7)	τ	110.81(7)
Tetrahedral ring distortion α		8.58(6)	
Octahedron *M*(1)		Octahedron *M*(2)	
M(1)−OH(1) (×2)	0.2064(1)	*M*(2)−OH(1)	0.2071(1)
M(1)−O(1) (×2)	0.2087(1)	*M*(2)−OH(1)	0.2073(1)
M(1)−O(2) (×2)	0.2090(1)	*M*(2)−O(1)	0.2081(1)
<*M*(1)−O>	0.2080	*M*(2)−O(1)	0.2088(1)
		M(2)−O(2)	0.2086(1)
		M(2)−O(2)	0.2087(2)
		<*M*(2)−O>	0.2081
Octahedron *M*(3)		Octahedron *M*(4)	
M(3)−OH(4)	0.2082(1)	*M*(4)−OH(2) (×2)	0.1938(1)
M(3)−OH(4)	0.2085(1)	*M*(4)−OH(3) (×2)	0.1944(1)
M(3)−OH(2)	0.2086(2)	*M*(4)−OH(4) (×2)	0.1934(1)
M(3)−OH(2)	0.2097(1)	<*M*(4)−O>	0.1939
M(3)−OH(3)	0.2086(2)		
M(3)−OH(3)	0.2092(1)		
<*M*(3)−O>	0.2088		
Sheet thickness		O−H bonds	
Tetrahedral	0.2342(1)	O(1)−H(1)	0.0967(2)
Octahedral	0.2159(2)	O(2)−H(2)	0.0870(3)
Interlayer*	0.1948(1)	O(3)−H(3)	0.0911(2)
Interlayer‡	0.3755(2)	O(4)−H(4)	0.0897(2)

* Interlayer thickness based on the oxygen atom positions
‡ Interlayer thickness based on hydrogen atom positions.

bi-dimensional matrix of Force Curves is acquired, which determined the force-field distributions above the sample. Two kinds of cantilever were used: a rectangular NanoWorld (Switzerland) EFM type conductive probe (nominal force constant k = 2.8 N/m) with a metallic Pt-Ir coating layer ~23 nm thick and a triangular-shaped Veeco NP type non conductive probe (nominal force constant k = 0.06 N/m), which was plated with a thin Au film ~10 nm thick. To improve the spatial resolution of the probes, the metallic coating was customized with a Focused Ion Beam (FIB) microscope (FEI Strata TM DB235). This microscope combines a high-resolution FIB column, which is equipped with a Ga liquid metal ion source, and a scanning electron microscopy column with a Schottky field emission electron gun. To localize the field, only an apical zone of the tip was covered with a conductive layer (~1 μm for the Veeco NP tip and ~3 μm for NanoWorld EFM tip). Thus, a conductive pathway was formed between the tip and the chip base (~3 μm wide for NP and, ~6 μm for NanoWorld EFM). To calibrate the cantilever's deflection *vs*. the tip–sample voltage difference, an atomically flat, cleaved graphite standard was used to avoid any morphological contribution to the signal. In Kelvin probe force microscopy (KPFM) mode, the surface potential was measured by using the conductive Veeco MESP tips (Antimony (n)-doped Si, Co/Cr coating, k ≈ 3 N/m, working frequency ≈ 80 kHz) and NCHPt-2 Nanoworld (Switzerland) Pt-Ir-coated silicon tips (k ≈ 42 N/m, working frequency ≈ 270 kHz).

DNA deposition

A linear, double-stranded λ-DNA of 48502 base-pair length was diluted with a K-glutamate buffer, 10 mM Tris HCl, and 1 mM EDTA, which dilution is commonly used for type-III restriction endonuclease (Fermentas Life Sciences, USA). The final DNA concentration was 1 nM, at pH 7.6 in ultra-pure water solution (Gibco, USA; Ultra-pure water DNAse, RNAse free). To assess the interactions of shorter DNA molecules, a 4331 base pairs plasmid DNA, linearized by a PstI restriction enzyme, was used at a concentration of 1 nM, at pH 7.6 in an ultra-pure water solution.

https://doi.org/10.1346/CCMN.2009.0570205 Published online by Cambridge University Press

The clinochlore surfaces under investigation were freshly cleaved and sterilized by a quartz sterilizer (Valdrè, 2007). Each surface of interest was characterized morphologically, to the nano-scale level, by SPM and determined to be free of contamination. Then, a 20-µL drop of the biological material was deposited on the surface. The samples were incubated for 5 min in a water-vapor-saturated environment, rinsed gently, washed for 30 s with ultra-pure water, and dried with an ultra-pure N_2 flow. This procedure was tested previously and produces well equilibrated DNA molecules on muscovite (Antognozzi *et al*., 2002; Valdrè *et al*., 2004).

RESULTS AND DISCUSSION

Crystal structure and chemistry

The structural refinement is in good agreement with that of Joswig and Fuess (1990) and highlights a partial ordering of trivalent cations in the interlayer with preference for the *M*(4) site. The <*M*(4)−O> mean bond length is 0.1939 nm, <*M*(3)−O> is 0.2088 nm, and <*M*(1)−O> and <*M*(2)−O> are 0.2080 and 0.2081 nm, respectively.

The tetrahedral cations are disordered, the <*T*(1)−O> and <*T*(2)−O> mean bond lengths being 0.1664 and 0.1661 nm, respectively. The tetrahedral rotation angle, α, defined as the difference between 120º and the Φ angles formed by the basal O−O edges of adjacent tetrahedra [$2\alpha = \Sigma_{i=1,6}(|120 - \Phi i|)/6$], is 8.58(6)º. The tetrahedral angles τ ($\tau = [\sum_{i=1}^{3}(O_{apical} - T - O_{basal})/3]$), $\tau_{T(1)}$ = 110.76(7)º, and $\tau_{T(2)}$ = 110.81(7)º suggest that both tetrahedra are elongated along **c*** (for an ideal tetrahedron, $\tau = \cos^{-1}(-1/3) \approx 109.47$º). The intralayer hydrogen bond O(1)−H(1) is 0.0967(2) nm. H-bond distances between OH of the interlayer and the tetrahedral basal O atoms are: O(2)−H(2) = 0.0870(3), O(3)−H(3) = 0.0911(2), and O(4)−H(4) = 0.0897(2) nm.

X-ray absorption spectroscopy

Comparison of XANES spectra (Figure 1) for clinochlore, tetra-ferriphlogopite, and annite revealed a sharp pre-edge peak characteric of tetra-ferriphlogopite, which contains Fe^{3+} in tetrahedral coordination, whereas this peak is absent in annite, which contains Fe^{2+} in octahedral sites. This peak represents an *s*-*d*-like transition and its intensity depends on the coordination environment and site symmetry of the absorber. The peak reaches a maximum for tetrahedral coordination and is absent for octahedral coordination (Waychunas, 1987; Wu *et al*., 2001). In clinochlore, a well defined

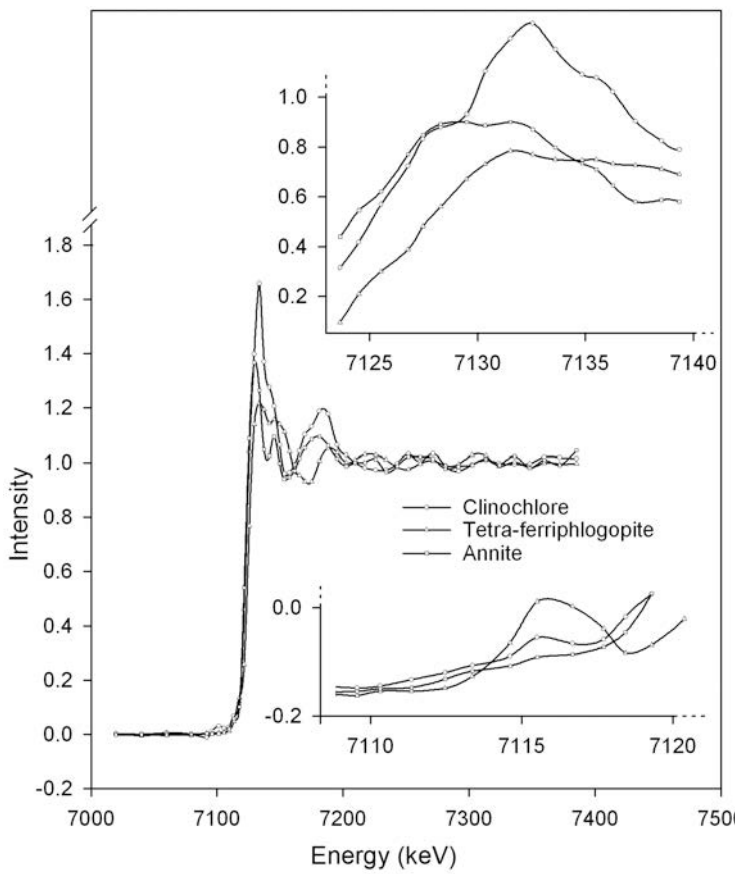

Figure 1. Fe *K*-XANES spectra of the clinochlore studied compared with those of tetra-ferriphlogopite and annite.

https://doi.org/10.1346/CCMN.2009.0570205 Published online by Cambridge University Press

peak at the same energy of tetra-ferriphlogopite suggests that Fe^{3+} is in tetrahedral sites. The edge energy value is related to the Fe oxidation state. The absence of a valence electron decreases the screening of core electrons and strengthens the core energy levels to produce an increase in the binding energy of the inner shell electrons (Wu *et al*., 1996).

The edge-energy position (E_0) is determined from the first derivative of the energy of the standard Fe metal foil. E_0 is 7123.7 eV in tetra-ferriphlogopite and 7121.5 eV in annite, indicating the presence of dominant Fe^{3+} and Fe^{2+}, respectively. In clinochlore, E_0 is at 7122.4 eV, which suggests the presence of Fe^{2+}. These results, however, are tentative because the XANES spectrum records the sum of the contributions of all the Fe atoms in the structure and assessing the presence of possible complex isomorphous structures is difficult.

The EXAFS refinement indicates that the first coordination shell of Fe is similar for clinochlore and annite (0.2055 and 0.2117 nm, respectively), thus suggesting octahedral Fe^{2+} in clinochlore. Fe-rich chlorite was previously characterized by Mössbauer spectroscopy and molecular orbital calculations by Lougear *et al.* (2000), who found that the calculated Fe–O bond charges increase in the following order: $M(1) < M(2) < M(3)$, suggesting that substitution of Mg^{2+} by Fe^{2+} is energetically more favorable for $M(3)$ than for $M(2)$ or $M(1)$ sites.

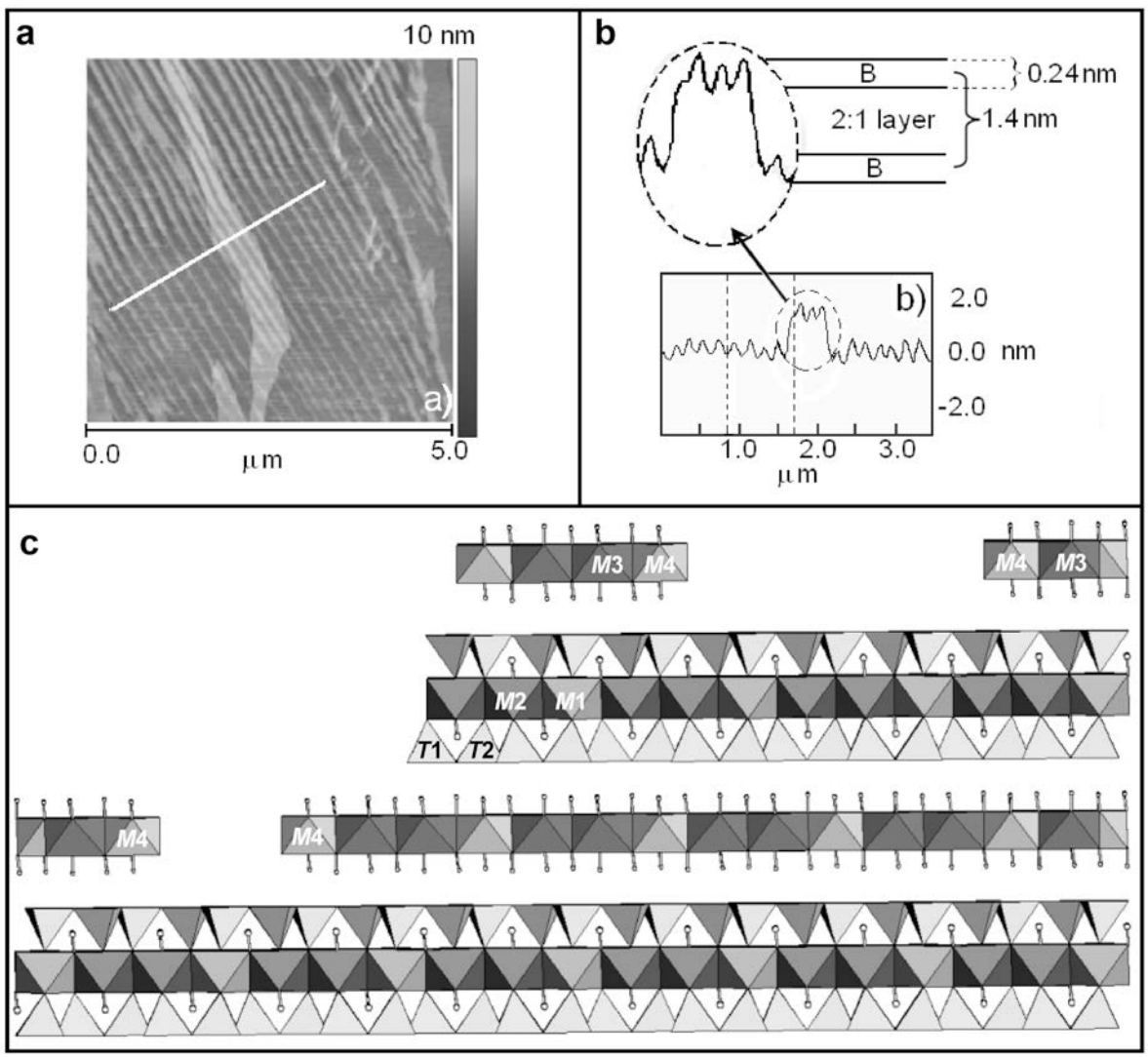

Figure 2. (a) Typical AFM topographic image of the clinochlore surface as cleaved. Octahedral interlayer remnants are recognizable as bright, narrow, parallel stripes (100 nm wide) over a dark background. (b) Profile section performed along the white line shown in (a); the interlayer (B) step is ~0.4–0.5 nm. Of note in the middle of the profile (see the enlargement inset) is an 'island' of a 2:1 layer ~1.0 nm thick, above which stand three interlayer stripes. The 2:1 layer lateral fracture shape is different from that of the interlayer. (c) Schematic structural interpretation of the cleaved surface.

https://doi.org/10.1346/CCMN.2009.0570205 Published online by Cambridge University Press

Cleavage nanotopography

Figure 2a shows a representative AFM topographic image of the (001) cleavage surface of clinochlore. The interlayer, consisting of Mg, Fe^{2+}, and Al cations and OH anions, appears as bright micrometer-long stripes over a darker background. The profile section along the white line in Figure 2a is shown in Figure 2b. The interlayer is ~0.4 nm thick, in good agreement with the SC-XRD results (interlayer thickness = 0.3775(2) nm). The direction of the stripes is along the [100] crystal direction and many near-parallel stripes, as much as several micrometers long, are observed. Statistically, the surface density of the two stripes (with and without the interlayer) are equal. Some stripes extend over islands of 2:1 layers (see the sketch of the profile in Figure 2b and a structural sketch in Figure 2c) but still parallel to stripes belonging to the interlayer below. The lateral fracture morphology of the 2:1 layer differs from that of the interlayer (Figure 2a).

The AFM images of other representative cleavage patterns of clinochlore show that several cleavage features can be distinguished (Figures 3 and 4). The surface shows missing interlayer regions that are triangular in shape (Figure 3), with average lateral sizes ranging from a few to more than hundreds of nanometers. The surface cleavage plane is characterized by the mixed presence of regions of triangular voids and stripe configurations (Figure 4). These cleavage features are not unique, but are general features that behave topotactically, *i.e.* appearing to be always identical, layer by layer, along a direction perpendicular to the basal plane (Figures 4, 5a). These features have been observed in hundreds of images in the present study.

The surface potential difference (ΔV) between the oxygen basal plane and the interlayer upper surface was estimated by KPFM and EFM surface potential analysis. The tip of the probe was kept at a constant height of 10 nm, and the measurements were performed at room temperature, atmospheric pressure, and relative humidity of 30–70%. The ΔV ranged from 50–100 to 400–500 mV depending on the relative humidity, which is known to influence the measurement because of the shielding effect of H_2O (Sugimura *et al.*, 2002) on the region under investigation. Figure 5b shows a Kelvin-probe surface-potential image of the topographic image of Figure 5a. The effective surface potential, ΔV, was determined to be ~70 mV. Consequently, in addition to the absolute value of ΔV, cleavage surfaces present atomically flat, nano-confined electrostatic potential gradients.

Oriented deposition of DNA onto the clinochlore surface

When the negatively charged molecules of DNA were deposited on a clinochlore surface, the surface showed areas of great DNA affinity, with ~50% surface coverage onto the positively charged interlayer. Areas where the DNA molecules were absent corresponded to the negatively charged basal oxygen plane of the 2:1 layer. This effect is the result of the asymmetric electrostatic layer structure of clinochlore which consists of a mixed surface of positive and negative areas.

Furthermore, the border between these regions is 'atomically' defined as it follows the layer topology. The DNA molecules tend to congregate at the boundary on the ledges (*i.e.* the fracture zone) of the interlayer, as shown by the topographic image (Figure 6a) and the

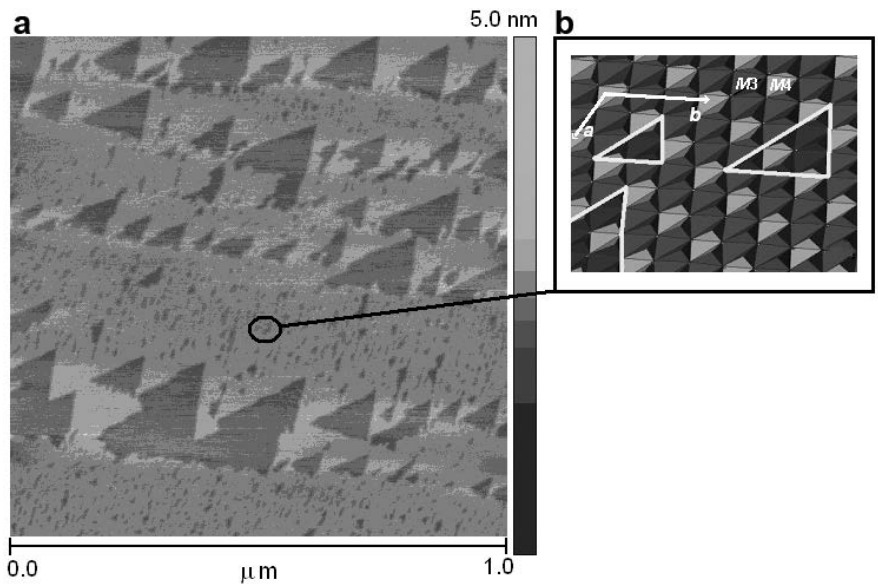

Figure 3. (a) AFM image of missing interlayer areas of typical triangular shape. (b) Schematic structural interpretation of the cleaved surface.

https://doi.org/10.1346/CCMN.2009.0570205 Published online by Cambridge University Press

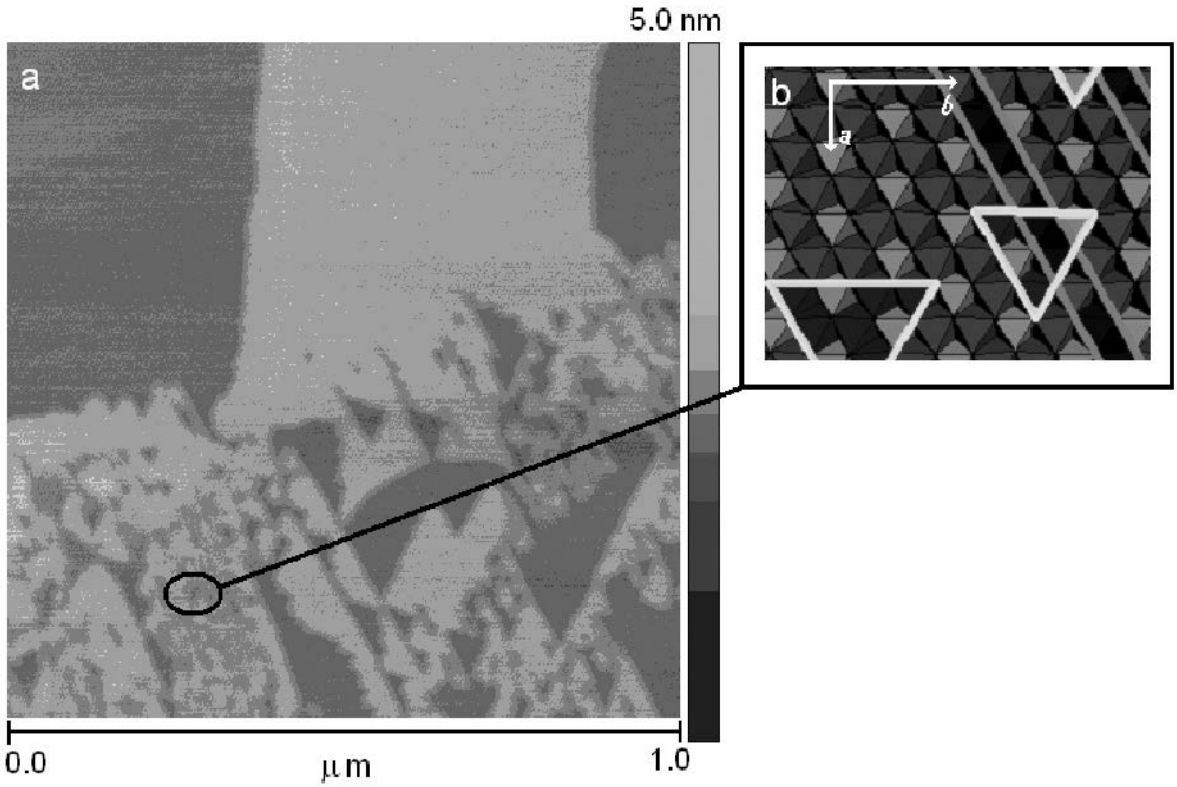

Figure 4. (a) AFM image of the mixed presence of both triangular and stripe-type cleavage patterns of clinochlore. (b) Schematic structural interpretation of the cleaved surface.

related profile perpendicular to the interlayer ledge (Figure 6b) after DNA deposition. This effect indicates that the surface potential at the ledge of the interlayer is greater than at the surface far removed from the ledge, suggesting that at the ledge, the most strongly bonded octahedral cations are statistically favored to resist cleavage. Because the interlayer involves two symmetry-independent octahedra ($M(3)$ and $M(4)$), the more

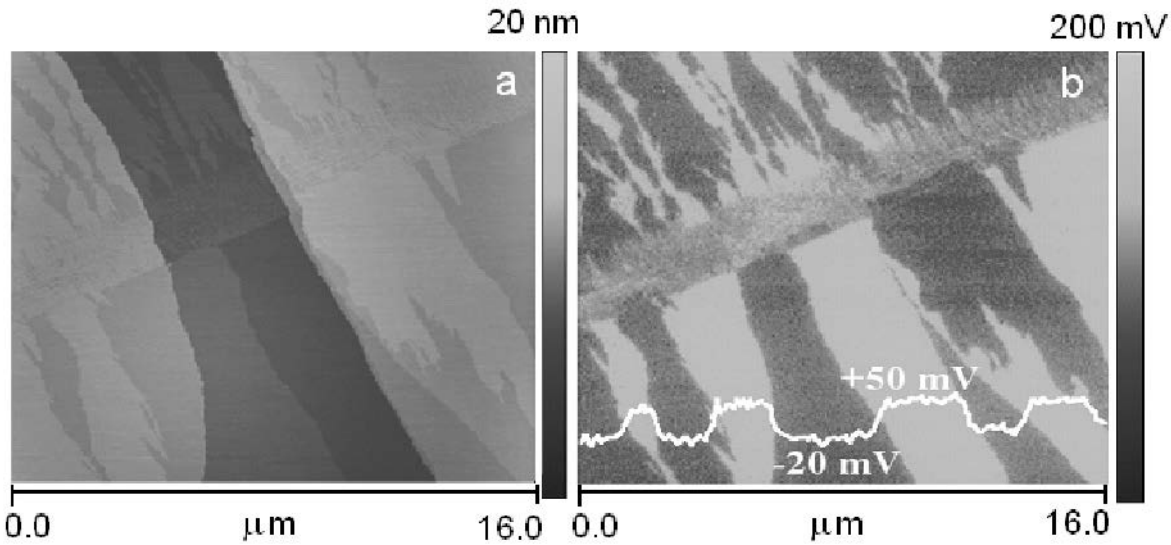

Figure 5. (a) AFM image of a cleavage area of the (00l) clinochlore surface where the same cleavage pattern is visible in the layers underneath the surface along a direction perpendicular to the basal plane. (b) Kelvin probe microscopy surface potential image of the surface shown in (a). Of note is the fact that the same surface potential difference, ΔV, is detected, independently of the basal plane considered.

https://doi.org/10.1346/CCMN.2009.0570205 Published online by Cambridge University Press

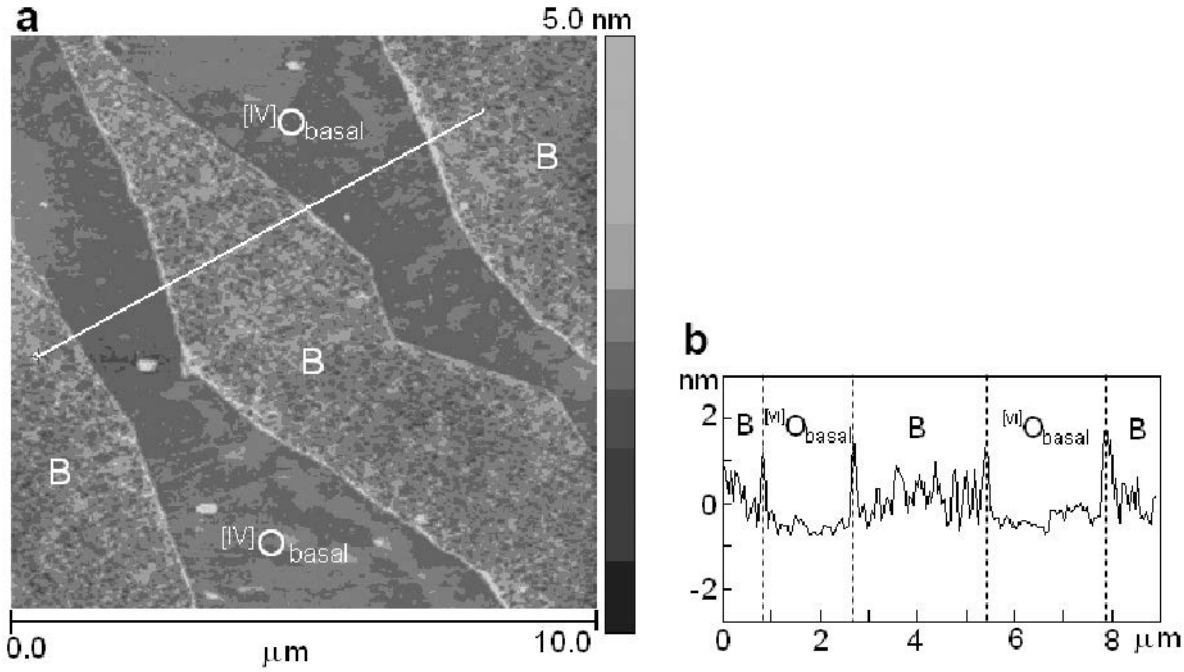

Figure 6. (a) AFM topographic image of the spontaneous selective deposition of DNA onto the interlayer surface of the clinochlore. (b) Profile analysis along the white line shown in (a). Of note is the systematic large concentration of DNA at the border of the interlayer regions. B: interlayer octahedral sheet surface; $^{[IV]}O_{basal}$: plane of tetrahedral basal oxygen atoms.

strongly bonded octahedra, *i.e.* those coordinated by Al^{3+} (*M*(4)), are probably more prevalent at the fracture sites of the interlayer.

The cleavage surface of clinochlore has adjacent regions each with either positive or negative potentials. The positive potential is ascribed to interlayer Mg, Fe^{2+} in *M*(3), and Al^{3+} in *M*(4). The AFM images show triangular and stripe-shaped irregularities, thus suggesting that the cleavage surface is fragmented along lines to form geometric figures.

An alternative explanation of the stripe-like and triangular cleavage pattern may be based in terms of the maximum bond density for the O–HO bonds between the interlayer octahedral sheet and the basal oxygen plane. The greatest density of basal oxygen atoms occurs along the [100] direction; thus more O–HO bonds are holding the interlayer in place along [100] and this may be the origin of the observed stripes along [100], involving the presence of the interlayer. The same arguments may apply to the formation of triangular pits because the least density of the O–HO bonds is at the ditrigonal ring of the 2:1 layer.

The importance of van der Waals interactions for DNA groove binding with other ligands has been raised by Chang and Cheng (1996), who proposed the role of hydrogen bonds to assist the appropriate orientation of the molecule. Agglomeration of DNA along the ledges could thus be explained by the combined effect of the positive charge on the vertical wall of clinochlore (interlayer octahedral sheet has a positive excess charge) and the van der Waals interactions which are the force that allows DNA crystals to form.

CONCLUSIONS

Clinochlore, after cleavage, presents a complex surface because the brucitic sheet, where cleavage occurs, is only partially covered by 2:1 layer islands. The interlayer thickness calculated from XRD data (0.3755(2) nm) is in good agreement with the value measured by AFM (~0.4 nm). As the interlayer surface is positive and the 2:1 layer is negative, the cleavage creates nano-confined high electric field gradients that can be exploited in various research and applied areas. For example, as shown here, the clinochlore is able to condense and order DNA filaments of 48502 and 4331 base pairs in length. Other studies reported that the surface anisotropy of chlorite was used to align DNA molecules for biotechnology purposes (Valdrè, 2005; Antognozzi *et al*., 2006; Valdrè, 2007). For practical applications, these specific substrates require the use of no binding agents or ligands, unlike other commonly employed substrates. In fact, the anisotropy of the electrostatic potential at the interlayer/oxygen basal plane boundary drives the alignment and condensation of DNA filaments in clinochlore. This anisotropy originates from the electrostatic potential arising from the positive charge of the interlayer octahedral sheet, particularly at the *M*(4) site. In addition, note that these mineral surfaces may present regions hundreds of

https://doi.org/10.1346/CCMN.2009.0570205 Published online by Cambridge University Press

micrometers long which may contain large numbers of Brønsted-Lewis active sites because of Al and Fe^{3+} in place of Si in tetrahedral sites and Al^{3+} and Cr^{3+} in the interlayer sheet.

The findings from this research offer new insights and perspectives in this complex interdisciplinary research field where the surfaces of phyllosilicates can be effective bioactive interfaces.

ACKNOWLEDGMENTS

The authors acknowledge valuable comments by S. Guggenheim. This research was supported by Italy's Ministero dell'Istruzione Università e Ricerca (MIUR) under the projects 'Micas: cation ordering, anionic composition as petrogenetic control factors' (PRIN 2006) and 'Progetti Strategici 2006,' of the University of Bologna. The authors also acknowledge Dr German Castro (Spanish Beam Line at ESRF, Grenoble) for his assistance in acquiring XAS spectra and the European Synchrotron Radiation Facilities (ESRF) for making beam time available.

REFERENCES

Antognozzi, M., Szczelkun, M., Round, A.N., and Miles, M.J. (2002) Comparison between shear force and tapping mode AFM – high resolution imaging of DNA. *Single Molecules*, **3**, 105–110.

Antognozzi, M., Wotherspoon, A., Hayes, J.M., Miles, M.J., Szczelkun, M.J., and Valdrè, G. (2006) A chlorite mineral surface actively drives the deposition of DNA molecules in stretched conformations. *Nanotechnology*, **17**, 3897–3902.

Bailey, S.W. (1988) Chlorites: structures and crystal chemistry. Pp. 347–403 in: *Hydrous Phyllosilicates (exclusive of micas)* (S.W. Bailey, editor). Reviews in Mineralogy, **19**, Mineralogical Society of America, Chantilly, Virginia.

Bayliss, P. (1975) Nomenclature of the trioctahedral chlorites. *The Canadian Mineralogist*, **13**, 178–180.

Bruker (2003a) *APEX2*. Bruker AXS Inc., Madison, Wisconsin, USA.

Bruker (2003b) *SAINT-IRIX*. Bruker AXS Inc., Madison, Wisconsin, USA.

Bustamante, C., Vesenka, J., Tang, C.L., Rees, W., Guthold, M., and Keller, R. (1992) Circular DNA molecules imaged in air by scanning force microscopy. *Biochemistry*, **31**, 22–26.

Chang, D.-K. and Cheng, S.-F. (1996) On the importance of van der Waals interaction in the groove binding of DNA with ligands: restrained molecular dynamics study. *International Journal of Biological Macromolecules*, **19**, 279–285.

Downs, R.T. and Hazen, R.M. (2004) Chiral indices of crystalline surfaces as a measure of enantioselective potential. *Journal of Molecular Catalysis A: Chemical*, **216**, 273–285.

Giuli, G., Paris, E., Wu, Z.Y., Brigatti, M.F., Cibin, G., Mottana, A., and Marcelli, A. (2001) Experimental and theoretical XANES and EXAFS study of tetra-ferriphlogopite. *European Journal of Mineralogy*, **13**, 1099–1108.

Ha, B.Y. and Liu, A.J. (1997) Counterion-mediated attraction between two like-charged rods. *Physical Review Letters*, **79**, 1289–1292.

Joshi, M.S. and Paul, B.K. (1977) Surface structures of trigonal bipyramidal faces of natural quartz crystals. *American Mineralogist*, **62**, 122–126.

Joshi, M.S., Kotru, P.N., and Ittiakhen, M.A. (1970) Studying dislocations in quartz by the hydrothermal-etching method. *Soviet Physics Crystallography*, **15**, 83–89.

Joswig, W. and Fuess, H. (1990) Refinement of a one-layer triclinic chlorite. *Clays and Clay Minerals*, **38**, 216–218.

Klinov, D., Dwir, B., Kapon, E., Borovok, N., Molotsky, T., and Kotlyar, A. (2006) Comparative study of atomic force imaging of DNA on graphite and mica surfaces. *American Institute of Physics Conference Proceedings*, **859**, 99–106.

Krause, M.O. and Oliver, J.H. (1979) Natural widths of atomic K and L Levels, K_α X-ray lines and several KLL Auger lines. *Journal of Physical and Chemical Reference Data*, **8**, 329–338.

Lougear, A., Grodzicki, M., Bertoldi, C., Trautwein, A.X., Steiner, K., and Amthauer, G. (2000) Mössbauer and molecular orbital study of chlorites. *Physics and Chemistry of Minerals*, **27**, 258–269.

Meyrowitz, R. (1970) New semi-microprocedure for determination of ferrous iron in refractory silicate minerals using a sodium metafluoroborate decomposition. *Analytical Chemistry*, **42**, 1110–1113.

Parsons, R. (1990) Electrical double layer: Recent experimental and theoretical developments. *Chemical Reviews*, **90**, 813–826.

Sheldrick, G.M. (2005) *SADABS*. Version 2.10. University of Göttingen, Germany.

Sheldrick, G.M. (1997) *SHELX-97*, *program for crystal structure determination*. University of Göttingen, Germany.

Sugimura, H., Ishida, Y., Hayashi, K., Takai, O., and Nakagiri, N. (2002) Potential shielding by the surface water layer in Kelvin probe force microscopy. *Applied Physics Letters*, **80**, 1459–1461.

Sushko, M.L., Shluger, A.L., and Rivetti, C. (2006) Simple model for DNA adsorption onto a mica surface in 1:1 and 2:1 electrolyte solution. *Langmuir*, **22**, 7678–7688.

Theng, H.H., Dove, P.M., Orme, C.A., and DeYoreo, J.J. (1998) The thermodynamics of calcite growth: A baseline for understanding biomineral formation. *Science*, **282**, 724–727.

Tombolini, F., Brigatti, M.F., Marcelli, A., Cibin, G., Mottana, A., and Giuli, G. (2002) Crystal chemical study by XANES of trioctahedral micas: the most characteristic layer silicates. *International Journal of Modern Physics B: Condensed Matter Physics, Statistical Physics, Applied Physics*, **16**, 1673–1679.

Valdrè, G. (2005) AFM observation of agglomerates, ordered structures and filaments after deposition of DNA nucleotides onto layer silicate mineral structures. *Scanning*, **27**, 100–102.

Valdrè, G. (2007) Natural nanoscale surface potential of clinochlore and its ability to align nucleotides and drive DNA conformational change. *European Journal of Mineralogy*, **19**, 309–319.

Valdrè, G., Antognozzi, M., Wotherspoon, A., and Miles, M.J. (2004) Influence of properties of layered silicate minerals on adsorbed DNA surface affinity, self-assembly and nanopatterning. *Philosophical Magazine Letters*, **84**, 539–545.

Vesenka, J., Guthold, M., Tang, C.L., Keller, D., Delaine, E., and Bustamante, C. (1992) A substrate preparation for reliable imaging of DNA molecules with the scanning force microscope. *Ultramicroscopy*, **42–44**, 1243–1249.

Waychunas, G.A. (1987) Synchrotron radiation XANES spectroscopy of titanium in minerals: Effects of titanium bonding distances, titanium valence, and site geometry on absorption edge structure. *American Mineralogist*, **72**, 89–101.

Wilson, A.J.C. and Prince, E., editors (1999) *International Tables for X-ray Crystallography, Volume C: Mathematical, physical and chemical tables* (2nd edition). Kluwer

Academic, Dordrecht, The Netherlands.

Wu, Z., Mottana, A., Marcelli, A., Natoli, C.R., and Paris, E. (1996) Theoretical analysis of X-ray absorption near-edge structure in forsterite, Mg_2SiO_4-*Pbnm*, and fayalite, Fe_2SiO_4-*Pbnm*, at room temperature and extreme conditions. *Physics and Chemistry of Minerals*, **23**, 193–204.

Wu, Z., Natoli, C.R., Marcelli, A., Paris, E., Seifert, F., Zhang, J., and Liu, T. (2001) Symmetry role on the pre-edge X-ray absorption fine structure at the metal K edge. *Journal of Synchrotron Radiation*, **8**, 215–217.

(*Received 10 June 2008; revised 25 November 2008; Ms. 0169; A.E. H. Dong*)